



Publication Year	2016
Acceptance in OA@INAF	2020-05-19T14:36:14Z
Title	FR II radio galaxies at low frequencies - I. Morphology, magnetic field strength and energetics
Authors	Harwood, Jeremy J.; Croston, Judith H.; Intema, Huib T.; Stewart, Adam J.; Ineson, Judith; et al.
DOI	10.1093/mnras/stw638
Handle	http://hdl.handle.net/20.500.12386/24962
Journal	MONTHLY NOTICES OF THE ROYAL ASTRONOMICAL SOCIETY
Number	458

FR II radio galaxies at low frequencies – I. Morphology, magnetic field strength and energetics

Jeremy J. Harwood,^{1*} Judith H. Croston,^{2,3} Huib T. Intema,^{4,5} Adam J. Stewart,⁶
Judith Ineson,² Martin J. Hardcastle,⁷ Leith Godfrey,¹ Philip Best,⁸ Marisa Brienza,^{1,9}
Volker Heesen,² Elizabeth K. Mahony,¹ Raffaella Morganti,^{1,9} Matteo Murgia,¹⁰
Emanuela Orrú,^{1,11} Huub Röttgering,⁴ Aleksandar Shulevski¹
and Michael W. Wise^{1,12}

¹*ASTRON, The Netherlands Institute for Radio Astronomy, Postbus 2, NL-7990 AA Dwingeloo, the Netherlands*

²*School of Physics and Astronomy, University of Southampton, Southampton SO17 1BJ, UK*

³*Institute of Continuing Education, University of Cambridge, Madingley Hall, Madingley, Cambridge CB23 8AQ, UK*

⁴*Leiden Observatory, Leiden University, PO Box 9513, NL-2300 RA Leiden, the Netherlands*

⁵*National Radio Astronomy Observatory, 1003 Lopezville Road, Socorro, NM 87801-0387, USA*

⁶*Astrophysics, University of Oxford, Denys Wilkinson Building, Keble Road, Oxford OX1 3RH, UK*

⁷*School of Physics, Astronomy and Mathematics, University of Hertfordshire, College Lane, Hatfield, Hertfordshire AL10 9AB, UK*

⁸*SUPA, Institute for Astronomy, Royal Observatory, Blackford Hill, Edinburgh EH9 3HJ, UK*

⁹*Kapteyn Astronomical Institute, University of Groningen, PO Box 800, NL-9700 AV Groningen, the Netherlands*

¹⁰*INAF, Osservatorio di Radioastronomia, Via della Scienza 5, I-09047 Selargius (Cagliari), Italy*

¹¹*Department of Astrophysics, Institute for Mathematics, Astrophysics and Particle Physics (IMAPP), Radboud University Nijmegen, PO Box 9010, NL-6500 GL Nijmegen, the Netherlands*

¹²*Astronomical Institute ‘Anton Pannekoek’, University of Amsterdam, Postbus 94249, NL-1090 GE Amsterdam, the Netherlands*

Accepted 2016 March 11. Received 2016 March 10; in original form 2015 November 25

ABSTRACT

Due to their steep spectra, low-frequency observations of Fanaroff–Riley type II (FR II) radio galaxies potentially provide key insights in to the morphology, energetics and spectrum of these powerful radio sources. However, limitations imposed by the previous generation of radio interferometers at metre wavelengths have meant that this region of parameter space remains largely unexplored. In this paper, the first in a series examining FR IIs at low frequencies, we use LOFAR (LOW Frequency ARray) observations between 50 and 160 MHz, along with complementary archival radio and X-ray data, to explore the properties of two FR II sources, 3C 452 and 3C 223. We find that the morphology of 3C 452 is that of a standard FR II rather than of a double-double radio galaxy as had previously been suggested, with no remnant emission being observed beyond the active lobes. We find that the low-frequency integrated spectra of both sources are much steeper than expected based on traditional assumptions and, using synchrotron/inverse-Compton model fitting, show that the total energy content of the lobes is greater than previous estimates by a factor of around 5 for 3C 452 and 2 for 3C 223. We go on to discuss possible causes of these steeper-than-expected spectra and provide revised estimates of the internal pressures and magnetic field strengths for the intrinsically steep case. We find that the ratio between the equipartition magnetic field strengths and those derived through synchrotron/inverse-Compton model fitting remains consistent with previous findings and show that the observed departure from equipartition may in some cases provide a solution to the spectral versus dynamical age disparity.

Key words: acceleration of particles – radiation mechanisms: non-thermal – galaxies: active – galaxies: jets – radio continuum: galaxies – X-rays: galaxies.

* E-mail: Jeremy.Harwood@physics.org

1 INTRODUCTION

1.1 Radio galaxies

Radio galaxies can be broadly grouped into two categories: the centre-brightened Fanaroff & Riley (1974) class I (FR I) and the edge-brightened class II (FR II) galaxies. FR IIs generally consist of three key structures: jets, lobes and hotspots, and are the more powerful of the two classes with typical 1.4 GHz luminosities greater than $\sim 10^{25} \text{ W Hz}^{-1}$ (Owen & Ledlow 1994). The largest extent of jets and lobes in established FR IIs are commonly observed on scales of tens of kiloparsecs (Alexander & Leahy 1987; Konar et al. 2006; Machalski, Jamrozy & Saikia 2009) to megaparsecs (Mullin, Hardcastle & Riley 2006; Machalski et al. 2008) in size and, as these lobes are in direct contact with their external environment, they are able to interact with both the intergalactic medium and, if located in clusters, the intracluster medium. However, many unanswered questions remain about the underlying dynamics and energetics of these powerful radio sources.

Radio galaxies are widely believed to play an important role in the evolution of galaxies and clusters (e.g. Bower et al. 2006; Croton et al. 2006; Fabian 2012; McNamara & Nulsen 2012; Morganti et al. 2013; Heckman & Best 2014). Their presumed ability to suppress star formation in models of galaxy evolution and to interact with their surrounding environment means that accurately determining the dynamics and energetics of these powerful outflows is vital if we are to understand the impact they have on how galaxies and clusters evolve over time. This work addresses important questions regarding the dynamics and energy content of two nearby, powerful FR II radio galaxies that are representative of the class. Specifically, we address the question of whether the lobes are overpressured relative to the external medium, and expanding supersonically. This question surrounding the dynamics also has a strong impact on the predicted scaling relation between jet power and radio luminosity (Godfrey & Shabala 2016), a key ingredient in studies of radio loudness and jet production (Sikora, Stawarz & Lasota 2007) as well as quantifying radio mode feedback (Croton et al. 2006).

Limitations imposed by the previous generation of radio interferometers have meant that the brightness distributions of radio galaxies are currently poorly determined at metre wavelengths. Such observations are particularly important in the study of steep spectrum emission which is not detectable at higher frequencies, and in determining the energy content and distribution of the lowest energy electrons. With the LOw Frequency ARray (LOFAR; van Haarlem et al. 2013) now fully operational, this is set to change. Consisting of $\sim 25\,000$ high-band (HBA, 110–240 MHz) and low-band (LBA, 10–90 MHz) dipole antennas arranged into 46 stations spread throughout northern and central Europe, LOFAR is currently the world’s largest connected interferometer, with baselines of up to ~ 1500 km providing broadband, high-resolution observations at low frequencies. LOFAR therefore now allows detailed low-frequency spectral and morphological studies of radio galaxies on resolved spatial scales to be undertaken, and has already begun to produce exciting new results both for well-known active radio galaxies (e.g. 3C 31; Heesen et al., in preparation) and previously unknown remnant radio galaxies (e.g. Shulevski et al. 2015; Brienza et al. 2016). Such investigations are a key step if we are to accurately determine the impact of powerful radio galaxies on their environment.

1.2 The energetics and magnetic field of FR II radio galaxies

It has long been known that equipartition between the energy density of the relativistic particles in the lobes of radio galaxies and that of the magnetic field lies close to the minimum energy density required for the observed synchrotron-emitting plasma in radio galaxies (Burbidge 1956). Assuming that these are the only two factors contributing to the energy density, the total energy content of a source can be determined solely via synchrotron emission at radio wavelengths; however, this has historically led to problems such as apparently underpressured radio lobes in seemingly expanding sources (e.g. Morganti, Oosterloo & Tsvetanov 1988; Hardcastle & Worrall 2000; Worrall & Birkinshaw 2000; Harwood, Hardcastle & Croston 2015). A more robust calculation of the total energy content of FR II sources can be obtained where high-resolution X-ray data are available. X-ray emission from the lobes of FR IIs is fairly common (e.g. Tashiro et al. 1998; Hardcastle & Worrall 2000; Isobe et al. 2002; Hardcastle et al. 2004) and is thought to be a result of the inverse-Compton process upscattering cosmic microwave background photons (iC/CMB; e.g. Hardcastle & Croston 2005; Kataoka & Stawarz 2005). As the iC/CMB emissivity does not depend on the magnetic field of the source, modelling of the combined synchrotron/inverse-Compton spectrum (constrained by measurements at radio and X-ray energies, respectively) can provide a more robust measure of the magnetic field strength (e.g. Croston et al. 2004, 2005).

One key assumption required for these models is the spectrum at low frequencies, as the magnetic field calculation involves scaling from the synchrotron-emitting electrons with $\gamma \sim 10^4$ to the inverse-Compton electrons with $\gamma \sim 10^3$. Whilst integrated flux densities at these wavelengths have long been available, the limited number of data points has meant that the spectrum of this emission must be assumed. As the spectrum of these sources is always relatively steep ($\alpha > 0.5$),¹ any significant change in this assumption can greatly impact on the derived energy content of the source. LOFAR observations therefore provide the ability to constrain these models and evaluate the previously used assumptions about low-frequency spectrum and magnetic field strength.

1.3 Outstanding questions addressed in this paper

In this paper, the first in a series examining FR II radio galaxies at low frequencies, we use LOFAR observations to explore the morphology, magnetic field strength and energetics of two powerful radio sources. We address three primary questions.

- (i) How does the morphology of FR II radio galaxies at LOFAR frequencies compare to previous studies at higher frequencies?
- (ii) What is the magnetic field strength of FR II radio galaxies and does it agree with that derived from equipartition?
- (iii) Do improved constraints placed on the low-energy electron distribution change our understanding of the energetics of FR II radio galaxies?

In Section 2, we give details of target selection, data reduction and the analysis undertaken. Section 3 presents our results and in Section 4 we discuss these findings in the context of the aims outlined above. Throughout this paper, a concordance model in which $H_0 = 71 \text{ km s}^{-1} \text{ Mpc}^{-1}$, $\Omega_m = 0.27$ and $\Omega_\Lambda = 0.73$ is used (Spergel et al. 2003).

¹ We define the spectral index such that $S \propto \nu^{-\alpha}$.

Table 1. List of target sources and galaxy properties. ‘Name’ and ‘IAU name’ list the 3C and IAU names of the galaxies. ‘Spectral index’ lists the low-frequency spectral index between 178 and 750 MHz, and ‘LAS’ the largest angular size of the source. The ‘Redshift’, ‘5 GHz core flux density’, ‘178 MHz flux density’, ‘Spectral index’ and ‘LAS’ column values are taken directly from the online version of the 3CRR data base (Laing, Riley & Longair 1983, [http://3crr.extragalactic.info/cgi/data base](http://3crr.extragalactic.info/cgi/data_base)).

Name	IAU name	Redshift	5 GHz core flux density (mJy)	178 MHz flux density (Jy)	Spectral index (178 to 750 MHz)	LAS (arcsec)
3C 452	J2243+394	0.081	130	59.3	0.78	280
3C 223	J0936+361	0.137	9.0	16.0	0.74	306

Table 2. Observation details. ‘Name’ lists the 3C name of the galaxies and ‘Array’ refers to the LOFAR array configurations used. ‘Frequencies’ lists the frequency coverage of the observations. ‘Target TOS’ lists the time on source at each frequency. ‘Calibrator TOS’ lists the time on source at each frequency for the corresponding ‘Flux calibrator’. ‘LOFAR project ID’ refers to the project identifier as used by the LOFAR archive search facility (<http://lofar.target.rug.nl/>).

Name	Array	Frequencies (MHz)	Target TOS (min)	Flux calibrator	Calibrator TOS (min)	LOFAR project ID	Observation start date
3C 452	HBA Inner	110–180	440	3C 48	110	LC0_012	2013 August 27
	LBA Outer	30–80	589	3C 48	589	LC0_012	2013 September 16
3C 223	HBA Inner	110–180	429	3C 196	78	LC0_012	2013 May 14
	LBA Outer	30–80	595	3C 196	600	LC0_012	2013 May 23

2 DATA REDUCTION AND SPECTRAL ANALYSIS

2.1 Target selection and observations

13 targets were observed as part of the surveys Key Science Project, cycle-0 nearby AGN proposal covering various stages in the life-cycle of radio-loud active galaxies. Of this sample, two nearby powerful radio galaxies for which complementary X-ray observations were available, 3C 223 and 3C 452, were suitable for the study of active FR II sources (Table 1). To ensure good UV coverage and sensitivity, 10 h observations were made of each target at HBA and LBA frequencies using the core and remote Dutch stations. At the time of these observations, this provided baselines out to 100 km which, at the lowest HBA frequency (110 MHz), give a resolution of ~ 7 arcsec.

Suitable flux calibrators were selected for each target from a list of reference sources (Scaife & Heald 2012) which, for HBA observations, were interlaced with the target observations at 11 min intervals. At LBA frequencies, where correcting for changes in the atmosphere and side lobe effects on short time-scales is extremely important, the calibrator source was observed concurrently with the target by using some of the available bandwidth to form a second beam on the sky which constantly monitors the calibrator source. A summary of the observational setup is given in Table 2.

2.2 Data reduction

The calibration of the data used in this paper follows the guidelines set out in the standard imaging cookbook;² however, as LOFAR data reduction is a relatively new process, we summarize here some of the key procedures and LOFAR specific functions that have been written for the handling of these low-frequency data.

One key difference in the dipole setup of LOFAR compared to observations using parabolic dishes is the need for the removal of bright radio sources. As LOFAR always sees the entire sky, the five brightest radio sources (Cassiopeia A, Cygnus A, Hydra A, Taurus A

and Virgo A) must be subtracted from the data if they are expected to interfere heavily with a given observation. These so-called A-team sources, the properties of which have been well characterized, are therefore removed in a process known as demixing prior to the data being made available to the end user. However, if this demixing is performed when interference from A-team sources is not present, the data quality can deteriorate. Prior to observation, simulations were therefore run in order to determine if the demixing of A-team sources was required. We found that at both LBA and HBA frequencies, Cygnus A and Cassiopeia A heavily affect the observations, and demixing of these sources was undertaken. To reduce the data sets to a manageable size, each sub-band was also averaged down to four, 48.8 kHz channels and to 5 (HBA) and 10 (LBA) second integration times by the LOFAR support staff prior to the data being made available.

Once complete, the 3C 223 and 3C 452 data were downloaded from the archive to the LOFAR cluster at Southampton University and the ASTRON CEP3 cluster, respectively. Due to the high volume of data produced by LOFAR (even after averaging), a complete manual reduction of observations is not desirable, and so initial calibration was carried out using the observatory pipeline (Heald et al. 2010). Within this pipeline, flagging of visibilities affected by radio frequency interference (RFI) was first performed on the demixed and averaged data using the AOfLAGger of Offringa et al. (2010). Amplitude calibration and phase solutions were then determined from the calibrator sources (Table 2) using BlackBoard Selfcal (BBS; Pandey et al. 2009), which accounts for variations of the LOFAR station beams, and the solutions applied. Models of the fields of view were then created using the Global Sky Model (Scheers 2011) function which uses the VLA Low-frequency Sky Survey (VLSS), Westerbork Northern Sky Survey (WENSS) and NRAO VLA Sky Survey (NVSS) surveys (Condon et al. 1994, 1998; Rengelink et al. 1997; Cohen et al. 2007) to determine the source properties. A phase-only calibration was then carried out using BBS, all solutions were transferred to the target source, the array beam applied, and a further round of automated flagging performed on the corrected data. Finally, the individual sub-bands of the LOFAR observations were concatenated using the New Default Pre-Processing Pipeline (NDPPP) package and a manual inspection of the data made. To obtain a reasonable number of data points across the frequency space, but

² <https://www.astron.nl/radio-observatory/lofar/lofar-imaging-cookbook/>

Table 3. Summary of HBA imaging parameters. ‘Parameter’ refers to the imaging parameter used in making of radio maps within this paper. ‘CASA name’ refers to the CASA parameter taking the value stated in the ‘Values’ column.

Parameter	CASA name	Value	Units
Polarization	STOKES	I	
Image size	IMSIZE	4096 4096	pixels
Cell size	CELL	1.4 1.4	arcsec
Weighting	ROBUST	−0.5	
Beam size	RESTORINGBEAM	7.0 7.0	arcsec
Multiscale	MULTISCALE	[0, 5, 15, 45]	pixels

also maintain a good signal-to-noise ratio, the data were concatenated into 4 MHz bands for 3C 452 and 7 MHz bands for 3C 223 at HBA frequencies. At LBA frequencies, both observations were severely affected by the ionosphere and so were unsuitable for our analysis, with the exception of a single 12 MHz band for 3C 223 centred at 52 MHz. Any remaining RFI was then flagged manually using CASA in the standard manner.

In order to further improve the image quality, direction-independent phase-only self-calibration was then performed on each data set. CASA was chosen as the preferred imaging and self-calibration tool in order to utilize the multifrequency synthesis algorithm with two Taylor series terms ($n_{\text{terms}} = 2$; Rau & Cornwell 2011), which scales the flux by a spectral index value fitted over the observed bandwidth, and multiscale cleaning which were not yet available to the LOFAR specific AWImager (Tasse et al. 2013). This has the advantage of both enhancing the image fidelity and significantly reducing the computing time required. While this removed the ability to correct for the attenuation of the LOFAR primary beam, from fig. 21 of van Haarlem et al. (2013) we see that at 150 MHz the sensitivity at a field radius of 30 arcmin remains >95 per cent of the peak response. The fact that the sources are located at the centre of the field of view and have a largest angular size of only around 5 arcmin means that any losses due to the sensitivity drop-off could safely be ignored. Unlike in the high-frequency regime, the LOFAR self-calibration strategy involves including only the core LOFAR stations and iteratively moving outwards to include longer baseline. This is due to the remote stations (i.e. the longest baselines) not being on the same clock leading to potential time offsets, and ensures that phase coherence is maintained. Due primarily to RFI, instrumental and ionospheric effects (particularly at the edge of the observing frequency), at HBA wavelengths only 6 of the 7 MHz bands for 3C 223 and 10 of the 4 MHz bands for 3C 452 between ~116 and 160 MHz were suitable for final imaging.

Once self-calibrated, the images were mapped at the resolution appropriate to the lowest LBA and HBA frequencies with a cell size one fifth of that value. Although within this paper we are only interested in the integrated fluxes of the sources, these parameters ensure that the images are well matched in resolution to allow a full spectral ageing analysis to be performed in the second paper in this investigation. A summary of parameters used for the imaging described in this section is shown in Tables 3 and 4. HBA images were also created using the full bandwidth centred at a frequency of 147 and 138 MHz for 3C 223 and 3C 452, respectively. The resulting HBA and LBA images are shown in Figs 1 and 2.

2.3 Synchrotron/inverse-Compton model fitting

As was discussed in Section 1.2, it is a common assumption that the relativistic particles in the lobes of radio galaxies and the magnetic

Table 4. Summary of LBA imaging parameters. ‘Parameter’ refers to the imaging parameter used in making of radio maps within this paper. ‘CASA name’ refers to the CASA parameter taking the value stated in the ‘Values’ column.

Parameter	CASA name	Value	Units
Polarization	STOKES	I	
Image size	IMSIZE	4096 4096	pixels
Cell size	CELL	7.0 7.0	arcsec
Weighting	ROBUST	−0.5	
Beam size	RESTORINGBEAM	49.7 35.4	arcsec
Position angle	RESTORINGBEAM	89.8	degrees
Multiscale	MULTISCALE	[0, 5, 15, 45]	pixels

field are the only contributing factors in determining the energy density of the lobes; however, there is no a priori reason to believe that the total energy content (the sum of the energy density in the radiating particles, the magnetic field and any non-radiating particles such as protons) is not significantly higher than the minimum energy condition. This has made estimates of the energy budget based on radio observations alone highly uncertain.

The availability of X-ray data for our target sources reduces this problem by allowing a determination of the magnetic field strength to be made free from the assumption of equipartition and minimum energy. The total losses suffered by particles emitting at radio wavelengths are a combination of inverse-Compton and synchrotron losses, which are proportional to the magnetic field strength in the lobes and the equivalent field of the CMB such that $B = \sqrt{B_{\text{lobe}}^2 + B_{\text{CMB}}^2}$. The equivalent field of the CMB scales with redshift as $B_{\text{CMB}} = 0.318(1 + z)^2$; hence, the energy losses of the particles due to inverse-Compton scattering at low redshifts only become important at low frequencies.

Conversely, the energy gained by the CMB photons is given by (Longair 2011)

$$\frac{dE}{dt} = \frac{4}{3} \left(\frac{E}{m_e c^2} \right)^2 \sigma_T u_{\text{CMB}}, \quad (1)$$

where u_{CMB} is the energy density of the CMB. The X-ray inverse-Compton emission is therefore dependent on only the supply of photons that will be upscattered, in this case the CMB, and the energy of the scattering particles. Provided that the spectrum of a source is well known at radio wavelengths (particularly at low frequencies), the 1 keV inverse-Compton X-ray emission can be combined with the magnetic field-dependent radio synchrotron emission to give constraints on the magnetic field strength of the source.

For FR IIs where the contribution from non-radiating particles is thought to be negligible (Wardle et al. 1998; Homan & Wardle 1999; Croston et al. 2005; Konar & Hardcastle 2013), and with the magnetic field now known, a more robust estimate of the energy density of the synchrotron-emitting plasma, hence total energy content of the lobes, can also be made. To investigate the energetics of our two sources, we therefore refitted the synchrotron/inverse-Compton models used by Croston et al. (2004, 2005), constrained by the new radio observations presented here. In addition to the LOFAR measurements, flux densities at 330 MHz and 1.4 and 8 GHz were included in the synchrotron/inverse-Compton modelling which, along with the X-ray flux, were taken to be the values measured by Croston et al. (2004, 2005). Archival low-frequency measurements were also included to extend our frequency coverage down to around 10 MHz for 3C 452 and 20 MHz for 3C 223. In order to constrain the spectrum of 3C 452 at LBA frequencies, we also include the integrated flux value presented by

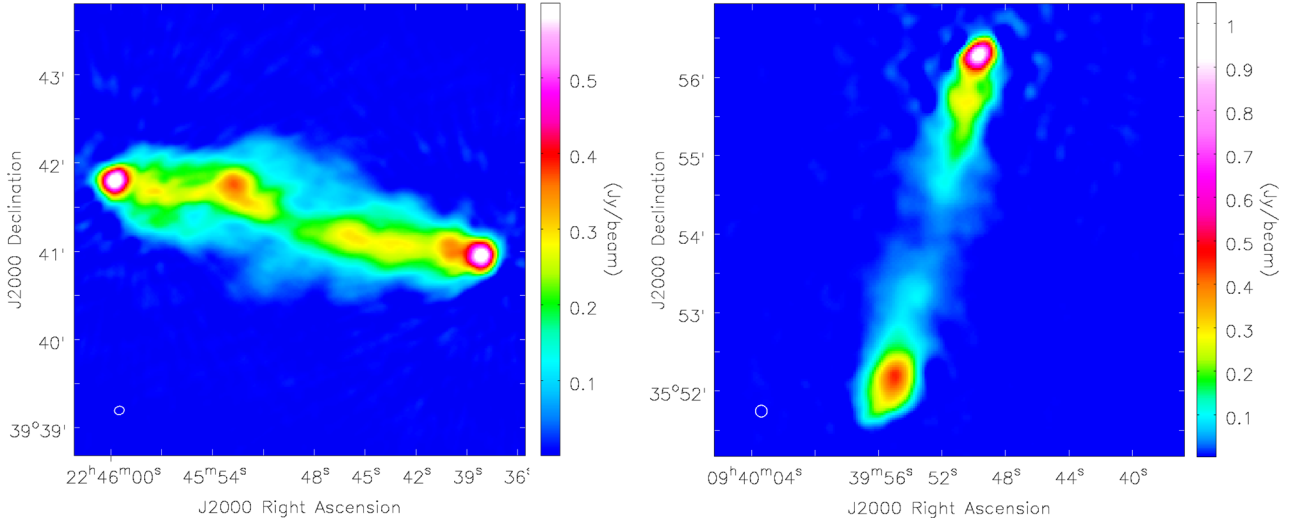


Figure 1. Radio maps of 3C 452 at 138 MHz (left) and 3C 223 at 147 MHz (right), imaged using multiscale CLEAN in CASA. The off-source rms noise is $0.45 \text{ mJy beam}^{-1}$ for 3C 452 and $0.48 \text{ mJy beam}^{-1}$ for 3C 223. The restoring beam is indicated in the bottom-left corner of the image.

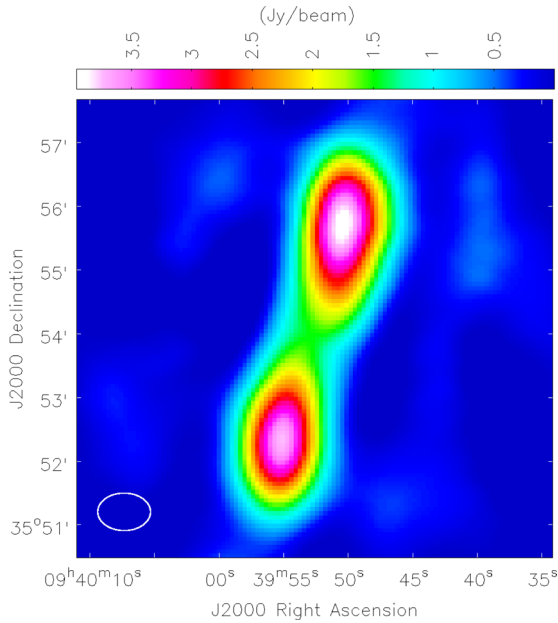


Figure 2. LOFAR LBA radio map of 3C 223 at 51.6 MHz with an off-source rms noise of $12.4 \text{ mJy beam}^{-1}$. The restoring beam is indicated in the bottom-left corner of the image.

Kassim et al. (2007) who use the Jansky Very Large Array (VLA) at 73.8 MHz assuming a 5 per cent uncertainty in the flux calibration. A summary of the archival data used is given in Table 5.

In order to ensure the results are directly comparable to those of Croston et al. (2005), 3C 452 uses the total flux for the model fitting as its morphology means there is no clear division between the two lobes. For 3C 223, the flux of each lobe was determined for the unresolved archival data using the ratio between the northern and southern lobes of 49:51 derived by Croston et al. (2004) who used the average of the fraction of the total flux in each lobe in the resolved images at 1.5 and 8 GHz.

The SYNCH code of Hardcastle, Birkinshaw & Worrall (1998a) was used to fit a two-component model consisting of a synchrotron spectrum constrained by low-frequency radio measurements and an

Table 5. Summary of archival data by frequency. ‘Frequency’ refers to the frequency at which measurements were made for each ‘Source’. The corresponding fluxes are listed in the ‘Integrated flux’ column with errors in the measurements shown in the ‘Uncertainty’ column. The ‘Reference’ column gives the origin of each value, denoted as follows: (1) Laing & Peacock (1980); (2) Kassim et al. (2007); (3) Croston et al. (2005); (4) Croston et al. (2004); (5) Leahy & Perley (1991); (6) Hardcastle et al. (1998b).

Source	Frequency (MHz)	Integrated flux (Jy)	Uncertainty (Jy)	Reference
3C 452	10	396.0	108.0	1
	22.3	331.2	21.7	1
	26.3	288.0	18.0	1
	38	236.0	70.8	1
	73.8	142.0	8.6	2
	86	114.0	3.0	1
	178	59.30	2.97	3
	1400	10.54	0.27	3
	8350	1.86	0.04	3
	3C 223	26.3	83.0	7.0
38		47.95	4.30	1
86		27.6	1.1	1
178		16.0	0.8	1
330		11.7	0.4	4
1477		3.49	0.07	5
8350		0.89	0.05	6

inverse-Compton spectrum constrained by X-ray observations. We applied the model presented by Croston et al. (2005) which used an electron distribution described by a single power law and bounded by the high- and low-energy cutoffs given in Table 6. The radio lobes were modelled as cylinders and we assumed a minimum energy cutoff where $\gamma_{\min} = 10$. This value is constant with that used by Croston et al. (2004, 2005) and was based on observations of hotspots in FR IIs where $\gamma_{\min} \sim 100$ to 1000 (e.g. Carilli et al. 1991; Hardcastle et al. 1998a) which, after adiabatic expansion (e.g. Godfrey et al. 2009), reduces to a γ_{\min} of approximately 10 for the lobes.

Table 6. Summary of synchrotron/inverse-Compton model parameters. ‘Parameter’ refers to the parameter name, where E_{\min} and E_{\max} are the assumed minimum and maximum energy of the electron distribution respectively and are taken directly from Croston et al. (2004, 2005). ‘Length, radius’ are the source dimensions assuming a cylindrical geometry and δ is the electron energy power-law index given by $\delta = 2\alpha_{\text{inj}} + 1$, where α_{inj} is the injection index of the source. Note that for 3C 452 we use the total size of the source, as opposed to the individual lobes, to allow direct comparison to the results of Croston et al. (2004, 2005).

Source	Parameter	Value	Units	Comments
3C 452	Length, radius	289.2, 89.0	arcsec	Total source
	δ	2.70		$\delta = 2\alpha_{\text{inj}} + 1$
	E_{\min}	5×10^6	eV	$\gamma \approx 10$
	E_{\max}	1×10^{11}	eV	$\gamma \approx 1 \times 10^6$
	3C 223	Length, radius	157.5, 21.5	arcsec
	Length, radius	152.0, 25.8	arcsec	Southern lobe
	δ	2.42		$\delta = 2\alpha_{\text{inj}} + 1$
	E_{\min}	5×10^6	eV	$\gamma \approx 10$
	E_{\max}	1×10^{11}	eV	$\gamma \approx 1 \times 10^6$

In theory, particles are shock accelerated in the hotspot regions of FR IIs to a power-law energy distribution such that

$$N(E) = N_0 E^{-\delta}. \quad (2)$$

The model parameter which describes the observed spectrum produced by this power-law distribution of shock-accelerated particles (the injection index) is directly related to the δ term by

$$\alpha_{\text{inj}} = \frac{\delta - 1}{2}. \quad (3)$$

For steep spectrum sources ($\delta > 2$) where $\gamma_{\max} \gg \gamma_{\min}$, a change in α_{inj} will have a significant impact on the energy stored at low frequencies scaling as

$$U_e \propto \frac{\gamma_{\min}^{2-\delta}}{\delta - 2}, \quad (4)$$

where U_e is the total energy contained in the relativistic electrons. For the special case where $\delta = 2$ ($\alpha_{\text{inj}} = 0.5$), the dependence on $\gamma_{\max}/\gamma_{\min}$ becomes logarithmic and so the impact on the total energy content is reduced.

The injection index was determined empirically from the best-fitting low-frequency spectral index of the LOFAR images and the measurements of Croston et al. (2004, 2005). As losses due to spectral ageing should be low at these wavelengths (discussed further in Section 4.3), this should provide a robust estimate of the initial power-law distribution.

3 RESULTS

3.1 Data quality and integrated flux

Before an analysis of these sources can be undertaken (particularly in the case of new instruments such as LOFAR), we must first consider the reliability of the calibration and any errors associated with the data. Comparison to previous studies provides a good check of our flux calibration. Using the integrated flux values and spectral index for 3C 223 presented by Orrú et al. (2010) who use VLA observations at 74 and 327 MHz and extrapolating to LOFAR LBA and HBA frequencies, we find total integrated flux values of 37.4 Jy at 51.6 MHz and 17.9 Jy at 161 MHz. As a secondary check, the same process can be carried out using the integrated fluxes tabulated by Laing & Peacock (1980) at 84 and 178 MHz. These give similar

Table 7. Summary of LOFAR maps by frequency. ‘Frequency’ refers to the frequency of the map, ‘Off-source rms’ refers to rms noise measured over a large region well away from the source. ‘Integrated flux’ values are listed at each frequency for the two lobes where ‘Lobe 1’ refers to the northern and eastern and ‘Lobe 2’ to the southern and western lobes of 3C 223 and 3C 452, respectively.

Source	Frequency (MHz)	Off-source rms (mJy beam ⁻¹)	Integrated flux (Jy)	
			Lobe 1	Lobe 2
3C 452	116.9	1.46	44.27	41.65
	121.8	1.41	43.39	40.96
	124.7	1.37	42.56	40.67
	128.6	1.28	41.87	39.90
	132.5	1.21	41.28	39.55
	136.4	1.23	40.06	38.88
	140.3	1.05	39.71	38.49
	152.0	1.08	38.07	37.10
	155.9	1.00	37.64	36.66
	159.9	0.947	37.15	36.30
3C 223	51.6	12.4	19.00	15.41
	118	1.08	13.69	11.0
	125	0.947	12.89	10.28
	133	0.910	12.03	9.76
	147	0.784	10.88	8.85
	154	0.840	10.38	8.40
	161	0.834	9.63	7.84

values of 36.9 Jy at 51.6 MHz and 17.0 Jy at 161 MHz. Following the same process for 3C 452 using the values of Nandi et al. (2010) at 153 MHz and the spectral index given by Hardcastle et al. (2004), we find that at 152 MHz the integrated flux is 81.6 Jy. Comparing these values to Table 7, and assuming a calibration error of 10 per cent at HBA and 15 per cent LBA frequencies due to uncertainties in the flux scale and global beam model (Scaife & Heald 2012; van Weeren, Williams & Tasse 2014), we find that our measurements are in good agreement with the literature. We note that for both sources the HBA in-band spectral index is flatter than one might expect given the overall spectrum between 50 MHz and 1.4 GHz. Uncertainties associated with the LOFAR HBA beam, particularly for measurements taken away from the central frequencies, mean that the in-band spectrum is currently still unreliable; however, the overall spectral index remains well within the stated calibration errors.

While the thermal noise measured in the images for both sources at HBA frequencies is relatively low ($\lesssim 1$ mJy beam⁻¹, Table 7), the noise close to the sources is significantly higher by a factor of around 5–10 times than when measured in a blank region of the sky. This increased noise is observed in both sources close to the hotspots and is therefore likely to be an issue related to dynamic range limitations in these regions. This is particularly prominent in the northern lobe of 3C 223 where the dynamic range is greatest. For the purposes of our analysis, the increased rms close to the source remains fractionally low compared to the integrated flux ($\lesssim 1$ per cent at HBA frequencies) and should therefore not impact significantly upon our results.

3.2 Morphology

From Fig. 1, we see that both 3C 223 and 3C 452 have a classical FR II morphology consisting of edge-brightened, diffuse lobe emission with clear hotspots towards the end of the source. The morphology of 3C 223 closely matches that of previous studies (e.g. Leahy & Perley 1991; Orrú et al. 2010) with previously known structure

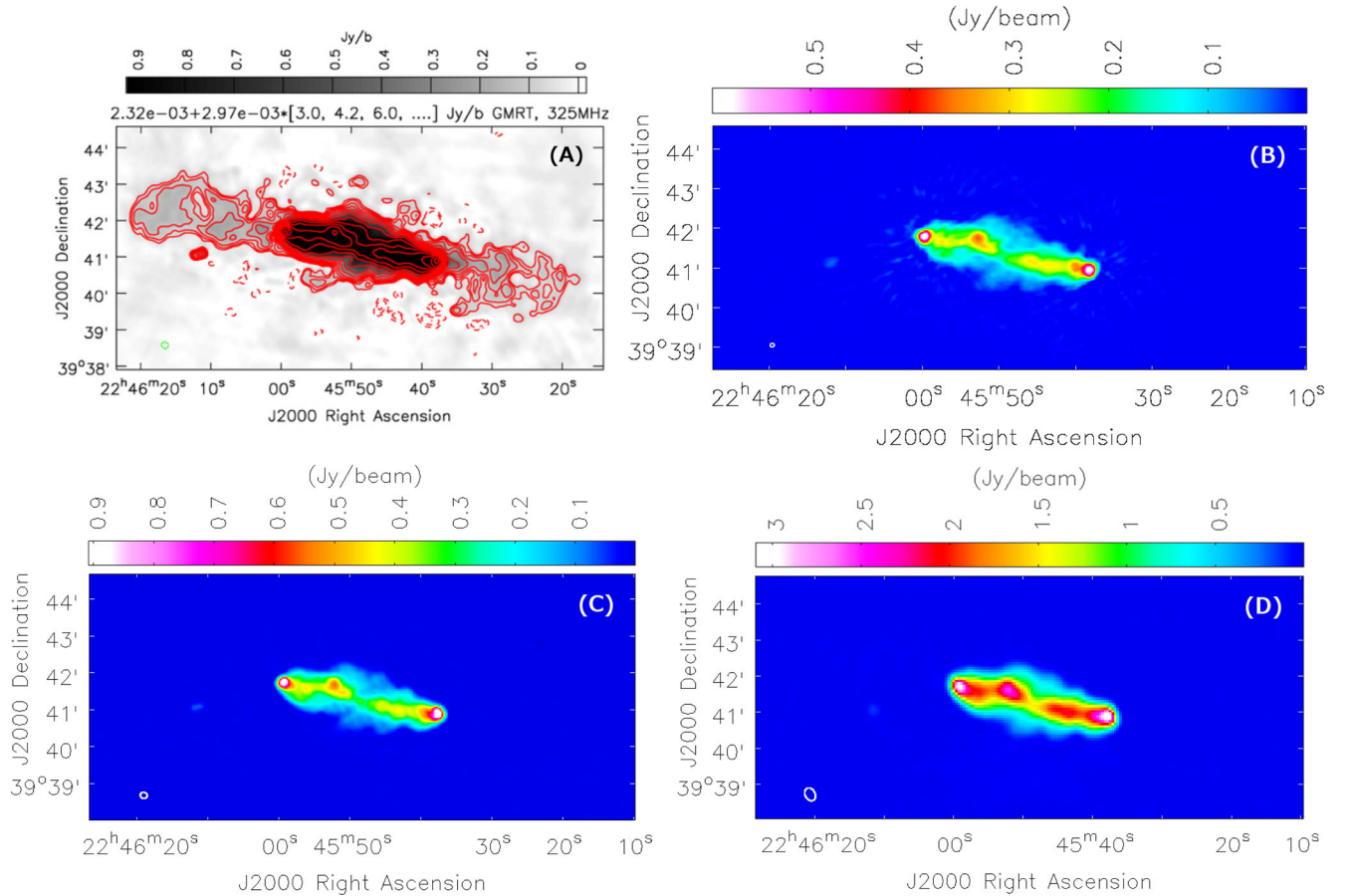


Figure 3. Radio maps of 3C 452 and the surrounding environment. (A) GMRT image at 325 MHz presented by Sirothia et al. (2013). (B) LOFAR full bandwidth HBA image at 138 MHz. (C) Reprocessing of the GMRT data used by Sirothia et al. (2013) at 325 MHz. (D) GMRT image at 153 MHz. All images are scaled to provide the same field of view. The restoring beams are indicated in the bottom-left corner of the images.

at comparable resolutions being successfully recovered. While for 3C 223 the observed morphology is what one would expect for a classical FR II, 3C 452 proves to be a more interesting case.

It was recently suggested by Sirothia, Gopal-Krishna & Wiita (2013) that 3C 452 may be a so-called double-double (DDRG; Schoenmakers et al. 2000). DDRGs contain two pairs of radio lobes resulting from two separate episodes of AGN activity: a pair of faint outer lobes from a previous active phase, and a pair of bright, inner lobes from the current outburst of activity. Panel A of Fig. 3 shows the image presented by Sirothia et al. (2013), where two pairs of these lobe-like structures are clearly visible, and the LOFAR image presented within this paper with a comparable field of view. While the active inner lobes of 3C 452 recover the same structure in both images, it is immediately clear that the outer remnant lobes are not observed in the LOFAR observations. We discuss the possible causes of this missing emission in Section 4.1.

3.3 Energy density and magnetic field strength

Within errors, the integrated LOFAR fluxes of both sources agree well with the original observations at other frequencies made by Croston et al. (2004, 2005); however, the now well-constrained spectrum of the emission at very low frequencies provides some potentially interesting differences with respect to the total energy content of the lobes of these sources. The integrated spectrum at these frequencies is much steeper than previously expected with

an index of 0.85 for 3C 452 and 0.71 for 3C 223, implying that a greater amount of energy is contained in the low-energy electron population than previously thought.

From Fig. 4, which shows the results of the synchrotron/inverse-Compton model fitting under the assumption that this steep spectral index is representative of the underlying initial electron energy distribution (Table 6), one finds that in order for the model to match the observed 1 keV inverse-Compton flux, an energy density of $1.2 \times 10^{-12} \text{ J m}^{-3}$ is required for 3C 452 and of 2.8×10^{-13} and $3.2 \times 10^{-13} \text{ J m}^{-3}$ are required for the northern and southern lobes of 3C 223, respectively (Table 8). Comparing these values to those presented by Croston et al. (2004, 2005), we find a change in the total lobe energy density by a factor of 5.0 for 3C 452 and by 2.3 in the northern and 2.0 in the southern lobes of 3C 223, a significant increase over previous estimates.

One consideration that should be made when determining the total energy content of the lobes is the uncertainty associated with γ_{\min} . While this value remains unconstrained, Croston et al. (2005) show that even if $\gamma_{\min} = 1000$ in the lobes, the effect on the total energy content is small, varying by only a factor of ≈ 2 for the injection index values used here. This is due to the electron energy spectrum's normalization increasing to maintain equipartition, so offsetting the reduction at the lowest energies and remaining consistent within the measurement errors. Therefore, while a significant shift in γ_{\min} could cause the total energy content of 3C 223 to be in closer agreement with previous estimates due to the injection index

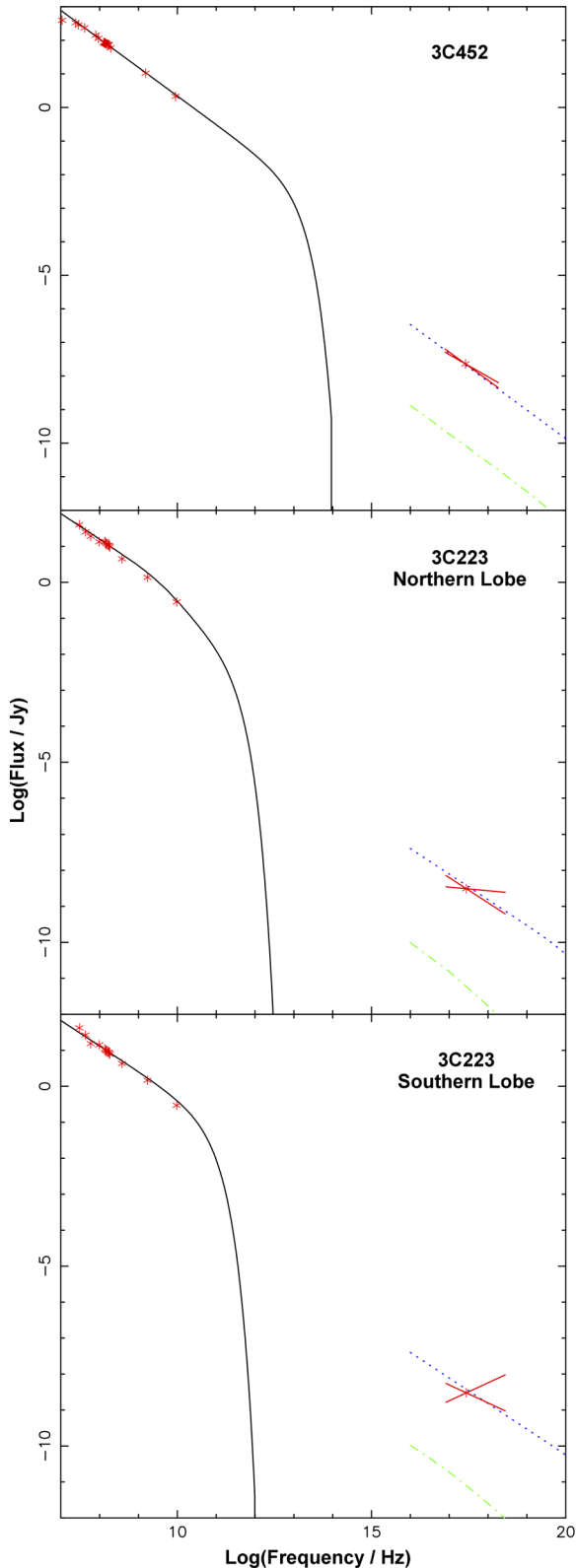


Figure 4. Synchrotron/inverse-Compton model fitting for 3C 452 (top), and the northern (middle) and southern (bottom) lobes of 3C 223. Red stars indicate the radio measurements fitted with a synchrotron spectrum (solid black line). The red bow tie indicates constraints placed by X-ray measurements with 1σ errors on the fitted inverse-Compton model (blue dotted line). The green dash-dotted line shows the expected location of the X-ray in the case of synchrotron self-Compton.

Table 8. Model fitting results. Synchrotron/inverse-Compton model fitting results assuming an intrinsically steep injection index of $\alpha_{inj} = 0.85$ and 0.71 for 3C 452 and 3C 223, respectively. ‘Magnetic field’ and ‘Energy density’ give the results for the region listed in the ‘Lobe’ column, where B_{iC} and B_{eq} give the magnetic field strength as derived from inverse-Compton measurements and equipartition, respectively.

Source	Lobe	Magnetic field (nT)		Energy density ($10^{-12} \text{ J m}^{-3}$)
		B_{iC}	B_{eq}	
3C 452	Total	0.45	0.87	1.2
3C 223	Northern	0.36	0.45	0.28
	Southern	0.32	0.45	0.32

of $\alpha_{inj} = 0.5$ assumed by Croston et al. (2004) scaling logarithmically (Section 2.3) rather than by equation (4), this is unlikely to be the case for 3C 452 where the difference is much larger.

The magnetic field strength is also affected by these revised estimates of the initial electron energy distribution. Comparing the results of Table 8 to those of Croston et al. (2004, 2005), we see an increase in the magnetic field strength of ~ 60 per cent for both 3C 452 and 3C 223. However, as a natural consequence the increased electron energy content at low frequencies also impacts on the equipartition value, causing it to increase from ~ 0.50 to 0.87 nT in 3C 452, and from ~ 0.35 to 0.45 nT in 3C 223. The values derived from X-ray constraints therefore remain lower than the equipartition value as originally shown by Croston et al. (2004, 2005). We discuss the implications of the steeper-than-expected low-frequency spectrum and the potential implications of the derived values further in Section 4.3.

4 DISCUSSION

The morphology and energetics of powerful radio galaxies play an important role in our understanding of the life-cycle of radio galaxies and the impact they have on their environment. Properties such as the total lobe energy content and magnetic field strength are key parameters which must be reliably determined if we are to derive properties such as source ages, lobe pressures and, ultimately, the total energy output of radio galaxies which can impact on galaxy evolution as a whole.

In this paper, we have presented results which explore the low-frequency morphology, energetics and integrated spectrum of two powerful radio galaxies, 3C 452 and 3C 223, which suggest a disparity from previous investigations. In the following section, we examine possible causes for our findings and their implications for our understanding of the FR II population.

4.1 Remnant emission in 3C 452

Until recently, 3C 452 was thought to be a prototypical example of an FR II-type radio galaxy with its strong hotspots and a classical morphology. This assertion was supported by observations presented by Nandi et al. (2010) who searched for remnant lobes using the Giant Metrewave Radio Telescope (GMRT; Swarup et al. 1991), but found no evidence for episodes of previous AGN activity. The discovery by Sirothia et al. (2013) that it may instead be a DDRG was therefore unexpected, with potentially significant consequences for models of radio galaxies, the unification of radio-loud AGN and their application in cosmological studies. The steep spectrum of remnant lobes makes low-frequency observations such as those used within this paper ideal for the study of such emission.

Table 9. Overview of GMRT observations of 3C 452. Details of the archival GMRT observations for 3C 452. ‘Frequency’ lists the central frequency at which the final images were made. ‘Target TOS’ list the observation length for the target and ‘Calibrator’ the source observed for flux calibration purposes. ‘rms’ lists the off-source noise and ‘Resolution’ the restoring beam of the final images.

Frequency (MHz)	Target TOS (min)	Calibrator	rms (mJy beam ⁻¹)	Resolution (arcsec)
153	370	3C 48	4.5	22.5 16.5
325	244	3C 48	1.7	11.3 10.0

Assuming a (very) conservative estimate for the spectral index for the outer lobes of $\alpha = 0.5$, correcting for the smaller LOFAR beam size and extrapolating the 3σ contour of Sirothia et al. (2013) back to 138 MHz, the faintest detected remnant emission should have a surface brightness of around 6 mJy beam⁻¹. If we assume the spectral index of 2.3 given by Sirothia et al., this increases to 27 mJy beam⁻¹, with brightest remnant regions being around 48 mJy beam⁻¹. This is well above the <1 mJy rms noise of the LOFAR images and so should be clearly visible but, as was noted in Section 3.2, this emission is not detected in our observations (Fig. 3).

In order to determine the cause of this missing emission, we reprocessed the 325 MHz GMRT data originally used by Sirothia et al. (2013) along with an additional observation at 153 MHz available in the GMRT archive under project code 13SPA01 (Table 9). We reduced these archival observations using the SPAM data reduction package (Intema et al. 2009). After initial flagging of strong RFI and dead antennas, flux, bandpass and instrumental phase calibrations were derived from the single scan on 3C 48 (adopting the flux standard as defined in Scaife & Heald 2012) and subsequently applied to the target field visibilities. Several iterations of self-calibration and wide-field imaging were started off with an initial phase-only gain calibration of the target field against a simple local sky model derived from NVSS, WENSS and VLSS. Each iteration also in-

cluded flagging of weaker but more abundant RFI. The resulting images were corrected for primary beam attenuation, small astrometric offsets and gain errors due to system temperature differences between flux calibrator and target field. From the resulting images shown in panels C and D of Fig. 3, we again see that the putative outer lobes are not detected at either frequency.

Additional information can also be gained by considering the integrated flux of the source. Fig. 5 shows the integrated spectrum of 3C 452 between 74 MHz and 1.4 GHz with the GMRT images presented within this paper and by Sirothia et al. (2013), alongside LOFAR and archival data. We see that within the errors, all measurements fall along a power law with the exception of the inner lobes of Sirothia et al. (2013). This is further reinforced by the fact that this value can be brought back into agreement when the fluxes from both the inner and outer lobes are combined, suggesting that flux from the inner lobes has at some point during the reduction process been shifted to form the outer lobes.

Given that the remnant emission should be easily observable at low frequencies but is not seen in either the LOFAR, GMRT 150 MHz or archival observations (e.g. Kassim et al. 2007, at 74 MHz), that we are unable to reproduce the additional diffuse structure presented by Sirothia et al. (2013) in the GMRT 330 MHz map, and that the integrated flux can be brought back into agreement when the integrated fluxes of the inner and outer lobes are combined, we conclude that the most probable cause of the observed outer lobes is artefacts introduced during the self-calibration and/or the imaging of the source. We therefore conclude that 3C 452 is not a DDRG, but is a standard FR II as was originally assumed.

4.2 Departure from equipartition

Equipartition between a source’s particle and magnetic field energy densities is a common assumption made in the study of radio galaxies in order to provide an estimate of the magnetic field strength but, as was described in Section 3.3, the addition of X-ray observations

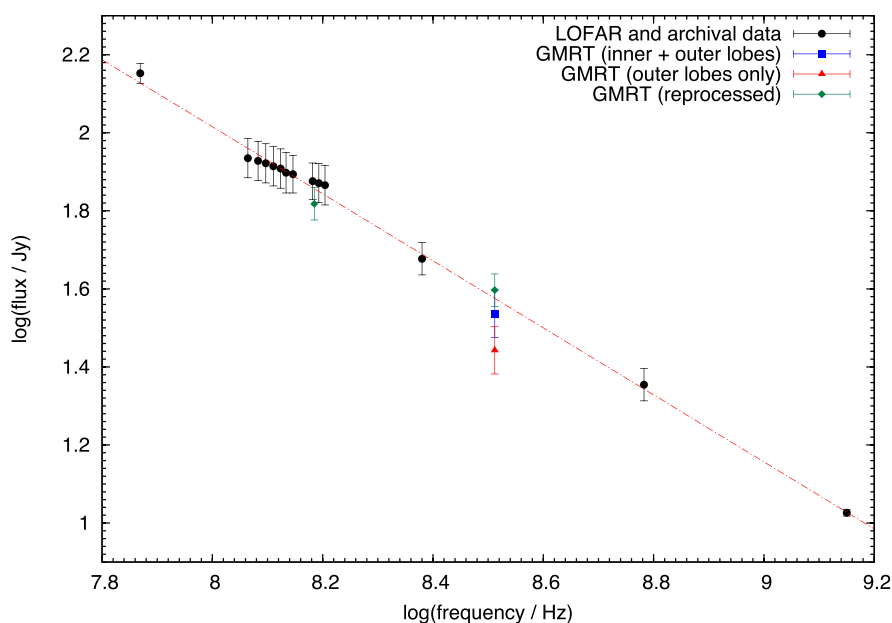


Figure 5. Integrated flux of 3C 452 between 74 MHz and 1.4 GHz. Black circles denote the LOFAR and archival data used in the synchrotron/inverse-Compton model fitting, with the dash-dotted line representing the best-fitting regression to these data. The red triangle indicates the flux of the inner lobes, and the blue square the combined flux of the inner and outer lobes as presented by Sirothia et al. (2013). The green diamonds show the values of the reprocessed GMRT data presented in this paper. Note that the upper error bar of the combined inner and outer lobe GMRT data passes through the reprocessed GMRT data point.

allows the value of the magnetic field strength to be determined free from this constraint. While for an intrinsically steep initial electron energy distribution (discussed further in Section 4.3) the absolute magnetic field strength increases by ~ 60 per cent compared to Croston et al. (2004, 2005), its relative strength remains much lower compared to equipartition irrespective of model, being only ~ 50 and ~ 75 per cent of the equipartition values for 3C 452 and 3C 223, respectively.

Deviation from equipartition is observed in similar FR II sources by Croston et al. (2004, 2005) and in 3C 452 by Shelton, Hardcastle & Croston (2011), who find $B \approx 0.3B_{\text{eq}}$ using inverse-Compton measurements independent of those of Croston et al. (2005). Such a difference therefore comes as no surprise, but as a consequence the ages of sources as derived from their spectrum are also affected. Spectral ageing, the preferential cooling of high-energy electrons due to synchrotron and inverse-Compton losses (Kardashev 1962; Pacholczyk 1970; Jaffe & Perola 1973; Tribble 1993), has long been used as a method of determining the age of radio galaxies and is a practice which continues to this day (e.g. Carilli et al. 1991; Jamroz et al. 2005; Orrú et al. 2010; Heesen et al. 2014; Brienza et al. 2016), but there is often a large discrepancy between the ages determined in this way and those determined from a dynamical view point (Eilek 1996; Harwood et al. 2013, 2015). In many cases, a simple solution to this problem is a weaker magnetic field strength, leading to lower radiative losses and older spectral ages. For example, in the case of 3C 438, a magnetic field strength of only $B \approx 0.5B_{\text{eq}}$ is required to bring the spectral age back into agreement with the dynamical age. However, in order to determine whether these departures from equipartition are able to provide the magnetic field strength required to bring the two ages into agreement for the population as a whole, a detailed ageing study of a large sample of radio galaxies where both X-ray and radio observations are available is required.

It is of course not feasible to use X-ray observations for all sources studied but, while the absolute magnetic field strength for both 3C 452 and 3C 223 is plausibly greater than previously estimated, the increased total energy density of the lobes also changes the equipartition value as a natural consequence of the assumed relationship between the two values. Consequently, the ratio between the equipartition value and that found from synchrotron/inverse-Compton model fitting for both 3C 452 and 3C 223 remains roughly constant, varying of the order of only 10 per cent. The results of Croston et al. (2005), who find a strong peak around a value of $0.7B_{\text{eq}}$, are therefore likely to be robust and provide a better estimate of the magnetic field strength in FR IIs than equipartition alone. Future studies using low-frequency radio surveys and the increased availability of archival X-ray observations will further refine this value, but these weaker field strengths may go at least part way to resolving the outstanding problem of explaining the spectrum of powerful radio galaxies. We suggest that such deviations should be carefully considered in future studies of FR IIs in order to provide a more accurate estimate of a source's age.

4.3 Energetics and lobe pressures

As the loss time-scale, τ , of an electron radiating via the synchrotron process scales as

$$\tau = \frac{E}{dE/dt} \propto 1/E \propto 1/v^2, \quad (5)$$

it is commonly assumed that for all but the oldest sources (i.e. those of the order of a few 100 Myr or more), the low-frequency spectrum of radio galaxy lobes maintains their original power-law

form, providing a proxy for the initial electron energy distribution. Previous studies of 3C 452 and 3C 223 (e.g. Nandi et al. 2010 for 3C 452; Orrú et al. 2010 for 3C 223) suggest that both sources fall well within the required age range for this assumption to be valid; however, the flux measurements presented in Section 3.3 show that the integrated spectrum at low frequencies is much steeper than the traditionally assumed injection index value of $\alpha_{\text{inj}} \approx 0.5$ ($\delta \approx 2.0$).³

One possible cause of this observed steeper-than-expected injection index is that the measured spectrum at LOFAR frequencies is not representative of the underlying electron energy distribution. This is expected if the source undergoes time-dependent adiabatic and radiative losses throughout its life (e.g. Murgia et al. 1999) and is supported by simulations of FR II radio galaxies that suggest that the integrated spectrum at these frequencies may be driven to steeper values due to changes in the magnetic field strength, mixing of electron populations and the environment as a function of time (Kapinska et al. 2015). Under such conditions, the spectrum would not provide a good proxy for the initial electron distribution, and typical models of spectral ageing which are applied to the integrated flux (e.g. CI models; Pacholczyk 1970) would not provide an accurate description of the particle energy spectrum leading to an unreliable measure of a source's intrinsic age. Indeed, the fact that for 3C 223 the X-ray spectral index (constrained by the bow ties of Fig. 4) appears flatter than the radio spectral index indicates that the electron energy distribution flattens towards lower energies. The X-ray photons are produced by electrons/positrons with $\gamma \sim 1000$, a factor of $\gtrsim 2$ less than those responsible for the radio emission in the LOFAR HBA band, and comparable to those radiating in the LBA band, assuming a magnetic field strength ~ 0.5 nT.

An alternative explanation is that a break in the spectrum occurs at much lower frequencies than is classically expected for an FR II radio galaxy. If this is the case, the spectrum may eventually flatten to injection index values closer to the expected value of 0.5, and the total energy content of the lobes will be in better agreement with those derived by Croston et al. (2004, 2005). The low-frequency archival observations used in the model fitting suggest that the integrated spectrum of both 3C 452 and 3C 223 remains steep down to ≈ 20 MHz, although the uncertainty on these measurements does allow for some moderate curvature to be present. Observations at the very lowest frequencies (≈ 10 MHz; Braude et al. 1970; Laing & Peacock 1980) are limited by their large error bars (≈ 25 per cent), and so it is not possible to conclusively determine whether a break at very low frequencies is present in the spectrum. Magnetohydrodynamic modelling suggests that producing integrated spectra with such a low-frequency break is possible (Hardcastle et al., in preparation), but requires a spectrum not typically described by models of spectral ageing and there is no easy physical interpretation as to why such a break would occur.

The most intuitive physical explanation for the steep low-frequency electron energy distribution observed in both 3C 452 and 3C 223 is a weaker-than-expected shock due to a slow moving jet, as may plausibly be the case for less powerful objects such as 3C 438 (Harwood et al. 2015). There has been some suggestion of a correlation between jet power and injection index (Konar &

³ It is interesting to note that these values also agree with the average low-frequency (178–750 MHz) integrated spectral index of the 3CRR sample (Laing et al. 1983) and those of Nandi et al. (2010) who find an injection index of 0.78 for 3C 452. There is also some evidence that the jets of FR IIs are slightly (but significantly) steeper than the expected $\alpha_{\text{inj}} = 0.5$ (Young et al. 2005; Laing & Bridle 2013).

Table 10. Summary of lobe pressures. Table of derived lobe pressures for 3C 452 and 3C 223, assuming the steep injection indices discussed in Section 4.3. ‘ P_{lobe} ’ refers to the pressure of the lobe listed in the ‘Lobe’ column. ‘ P_{ext} ’ is the external pressure taken from Shelton et al. (2011) for 3C 452 and Croston et al. (2004) for 3C 223. ‘Ratio’ is the ratio of the lobe to external pressures.

Source	Lobe	P_{lobe} (Pa)	P_{ext} (Pa)	Ratio
3C 452	Total	4.0×10^{-13}	1.11×10^{-13}	3.60
3C 223	Northern	9.3×10^{-14}	9.6×10^{-14}	0.97
	Southern	1.1×10^{-13}	9.6×10^{-14}	1.15

Hardcastle 2013) with weaker shocks resulting in a steeper initial electron energy distribution; however, the strong, bright, compact hotspots observed in both 3C 452 and 3C 223 mean that this is unlikely to be the case. It is therefore more plausible that the emission results from a fast jet. It is theoretically possible to produce a high injection index under certain conditions through models such as those presented by Konar & Hardcastle (2013), although further investigation is required to determine if this is intrinsically the case.

Support in favour of an intrinsically steep injection index also comes from the spatially resolved spectra of FR II radio lobes. Harwood et al. (2013, 2015), who consider the spectrum of four other FR II radio galaxies on smaller spatial scales, find that in all cases the injection index is also steeper than previously assumed. These studies attempt to account for low-frequency curvature when determining the injection index (hence electron energy distribution) of a source and, due to being well resolved, should be relatively unaffected by the superposition of spectra due to limited resolution. Injection index values found in this way agree well with the low-frequency spectral indices presented in this paper and have proved robust against simulations (e.g. Stroe et al. 2014). We note that preliminary tests (which will form part of Paper II of this series) also find a similar distribution using the methods of Harwood et al. (2013, 2015) implemented in the BRATS⁴ software package; however, a similar assumption is made that the injection index is constant over the lifetime of the source. As simulations of FR IIs are currently unable to trace the spatial evolution and mixing of the underlying electron population, it is not yet clear on what scales such variations exist and to what extent this impacts upon the determination of injection index values determined in this way, but further developments should make this possible over the next few years.

A physically plausible argument can therefore be made for an intrinsically steep injection index which, if correct, would have a significant impact on our understanding of the energetics of FR II galaxies. Assuming no significant flattening of the spectrum at frequencies $\lesssim 20$ MHz, we can infer that a greater electron population is present at very low energies than previously assumed, resulting in the total energy content of the lobes increasing by a factor of between 2 and 5 compared to previous findings (Table 8). Using the standard equation for a relativistic plasma, $P_{\text{lobe}} = U/3$, where P_{lobe} is the lobe pressure and U is the total energy density, we see a significant change in the estimated internal pressure of the lobes (Table 10). Comparing these values to the external pressures at the tip of the lobes derived by Shelton et al. (2011) of $1.1 \pm 0.1 \times 10^{-13}$ Pa for 3C 452 and by Croston et al. (2004) of $9.6 \pm_{8.8}^{38.3} \times 10^{-14}$ Pa for 3C 223, we see that they are overpressured by a factor of about

4 for 3C 452, with the lobes of 3C 223 being approximately in pressure balance with the external medium.

For these revised values, our results for 3C 452 broadly agree with those of Shelton et al. (2011) who also find that the lobes are overpressured; however, our revised estimate of the total energy content increases the internal overpressure by a factor of 2 compared to their findings. Using the standard equation relating the Mach number of the shock, M , to the internal-to-external pressure ratio (Longair 2011) and rearranging in terms M , we find

$$M = \frac{\sqrt{2((\gamma_{\text{sh}} + 1)P_{\text{ext}} + (\gamma_{\text{sh}} - 1)P_{\text{int}})}}{2\sqrt{\gamma_{\text{sh}}}\sqrt{P_{\text{int}}}}, \quad (6)$$

where P_{ext} and P_{int} are the external and internal pressures and, for a monatomic gas, $\gamma_{\text{sh}} = 5/3$ is the ratio of specific heats. This gives a Mach number of $M = 1.8$ implying that the lobes are expanding supersonically and driving a shock as the lobes push through the external medium. Although such a relatively weak shock is unlikely to be observable with current X-ray instruments, a temperature increase is observed in the external medium just beyond the tip of the lobes (region 3 of Shelton et al. 2011). We can therefore be fairly confident that the lobes are both intrinsically overpressured and expanding through the external medium supersonically.

For 3C 223, our results once again agree within errors to those of Croston et al. (2004) with the tip of the lobe being at minimum in pressure balance with the external medium. While the results presented in this paper suggest that the internal pressure of the lobes may be significantly higher than those derived by Croston et al. (2004), the large uncertainty on the X-ray measurements from which the external pressure is derived means that both the overpressured and pressure balance cases are plausible. If one is to obtain the ratio of internal to external pressures to a higher degree of accuracy (e.g. to test the case of overpressured lobes), then improved X-ray measurements are required. While we cannot therefore rule out either case, this pressure increase supports the interpretation of Croston et al. (2004) that the source does, at minimum, have the required internal pressure to support the observed lobes. This is in line with other recent investigations into the pressure balance of FR IIs (Ineson et al., in preparation) which suggest that, while some exceptions are observed (e.g. 3C 444; Croston et al. 2011), the FR II population as a whole is at minimum in pressure balance with the external medium when the magnetic field strength is derived from synchrotron/inverse-Compton model fitting.

From the results presented in this paper, it is clear that a revision in our understanding of radio galaxy lobes at LOFAR frequencies is required. Either the low-energy electron population is much greater than previously assumed or new models describing the emission from the lobes of radio galaxies are required if we are to accurately determine the dynamics and energetics of FR II radio galaxies.

5 CONCLUSIONS

In this paper, we have presented a low-frequency study of two FR II sources, 3C 452 and 3C 223. Using LOFAR and complementary archival observations, we have explored the morphology of these sources and, by constraining the integrated spectrum between ~ 10 and 8000 MHz, have investigated their energetics. We have used synchrotron/inverse-Compton fitting to test two possible models of the low-energy electron population and, for the case of an intrinsically steep injection index, provided revised estimates of the magnetic field strength, total energy content and pressure of the

⁴ <http://www.askanastronomer.co.uk/brats>

radio lobes. We went on to discuss the impact of these findings on the pressure balance with the external medium. The key points made within this paper are as follows.

(i) The morphology of 3C 452 is that of a standard FR II-type radio galaxy, contrary to the DDRG classification of Sirothia et al. (2013).

(ii) In order to fit the low-frequency spectrum, either the injection index must be steeper than previously assumed or a break must be present at very low frequencies.

(iii) For an intrinsically steep initial electron energy distribution, we provide revised total energy content estimates which are between a factor of 2 and 5 greater than previous findings.

(iv) For these revised values, we find that the magnetic field strength of both sources is greater by around 60 per cent compared previous estimates, with values of 0.45 nT for 3C 452 and 0.36 and 0.32 nT for the northern and southern lobes of 3C 223, respectively.

(v) The ratio between equipartition fields and those derived through synchrotron/inverse-Compton model fitting remains consistent with previous findings at 0.50 and 0.75 for 3C 452 and 3C 223, respectively.

(vi) We suggest that the observed departure from equipartition may, in some cases, provide a solution to the spectral versus dynamical age disparity problem.

We therefore conclude that the morphologies of both 3C 452 and 3C 223 are that of classical FR II galaxies, but with an integrated low-frequency spectrum steeper than has previously been assumed. We will further investigate these findings and the spectrum of these sources on resolved spatial scales in the second paper in this series.

ACKNOWLEDGEMENTS

We wish to thank the anonymous referee, Francesco de Gasperin, Clive Tadhunter, Peter Barthel and George Heald, for their constructive comments which have helped improve this paper. JJH wishes to thank the Netherlands Institute for Radio Astronomy (ASTRON) for a postdoctoral fellowship. This research was partly funded by the European Research Council under the European Union's Seventh Framework Programme (FP/2007-2013)/ERC Advanced Grant RADIOLIFE-320745. JHC, MJH and PNB are grateful for support from the Science and Technology Facilities Council under grants ST/M001326/1, ST/M001008/1 and ST/M001229/1. HTI acknowledges support from the National Radio Astronomy Observatory, a facility of the National Science Foundation operated under cooperative agreement by Associated Universities, Inc. AS is grateful for support from the European Research Council Advanced Grant 267697 *4 π sky: Extreme Astrophysics with Revolutionary Radio Telescopes*. The Low Frequency Array was designed and constructed by ASTRON (Netherlands Institute for Radio Astronomy), and has facilities in several countries, which are owned by various parties (each with their own funding sources), and which are collectively operated by the International LOFAR Telescope (ILT) foundation under a joint scientific policy. We thank the staff of the GMRT that made these observations possible. GMRT is run by the National Centre for Radio Astrophysics of the Tata Institute of Fundamental Research. This research has made use of the NASA/IPAC Extragalactic Database (NED), which is operated by the Jet Propulsion Laboratory, California Institute of Technology, under contract with the National Aeronautics and Space Administration.

REFERENCES

- Alexander P., Leahy J. P., 1987, *MNRAS*, 225, 1
- Bower R. G., Benson A. J., Malbon J. C., Helly J. C., Frenk C. S., Baugh C. M., Cole S., Lacey C. G., 2006, *MNRAS*, 370, 645
- Braude S. Y., Lebedeva O. M., Megn A. V., Ryabov B. P., Zhouck I. N., 1970, *Astrophys. Lett.*, 5, 129
- Brienza M. et al., 2016, *A&A*, 585, 29
- Burbidge G. R., 1956, *ApJ*, 124, 416
- Carilli C., Perley R., Dreher J., Leahy J., 1991, *ApJ*, 383, 554
- Cohen A. S., Lane W. M., Cotton W. D., Kassim N. E., Lazio T. J. W., Perley R. A., Condon J. J., Erickson W. C., 2007, *AJ*, 134, 1245
- Condon J. J., Broderick J. J., Seielstad G. A., Douglas K., Gregory P. C., 1994, *AJ*, 107, 1829
- Condon J. J., Cotton W. D., Greisen E. W., Yin Q. F., Perley R. A., Taylor G. B., Broderick J. J., 1998, *AJ*, 115, 1693
- Croston J. H., Birkinshaw M., Hardcastle M. J., Worrall D. M., 2004, *MNRAS*, 353, 879
- Croston J. H., Hardcastle M. J., Harris D. R., Belsole E., Birkinshaw M., Worrall D. M., 2005, *ApJ*, 626, 733
- Croston J. H., Hardcastle M. J., Mingo B., Evans D. A., Dicken D., Morganti R., Tadhunter C. N., 2011, *ApJ*, 734, L28
- Croton D. J. et al., 2006, *MNRAS*, 365, 11
- Eilek J. A., 1996, in Hardee P. E., Bridle A. H., Zensus J. A., eds, *ASP Conf. Ser. Vol. 100, Energy Transport in Radio Galaxies and Quasars*. Astron. Soc. Pac., San Francisco, p. 281
- Fabian A. C., 2012, *ARA&A*, 50, 455
- Fanaroff B. L., Riley J. M., 1974, *MNRAS*, 167, 31p
- Godfrey L., Shabala S., 2016, *MNRAS*, 456, 1172
- Godfrey L. E. H. et al., 2009, *ApJ*, 695, 707
- Hardcastle M. J., Croston J. H., 2005, *MNRAS*, 363, 649
- Hardcastle M. J., Worrall D. M., 2000, *MNRAS*, 319, 562
- Hardcastle M. J., Birkinshaw M., Worrall D. M., 1998a, *MNRAS*, 294, 615
- Hardcastle M. J., Alexander P., Pooley G. G., Riley J. M., 1998b, *MNRAS*, 296, 445
- Hardcastle M. J., Harris D. E., Worrall D. M., Birkinshaw M., 2004, *ApJ*, 612, 729
- Harwood J. J., Hardcastle M. J., Croston J. H., Goodger J. L., 2013, *MNRAS*, 435, 3353
- Harwood J. J., Hardcastle M. J., Croston J. H., 2015, *MNRAS*, 454, 3403
- Heald G. et al., 2010, *Proc. ISKAF2010 Science Meeting, ISKAF2010, Progress with the LOFAR imaging pipeline*. SISSA, Trieste, PoS#057
- Heckman T. M., Best P. N., 2014, *ARA&A*, 52, 589
- Heesen V., Croston J. H., Harwood J. J., Hardcastle M. J., Ananda H., 2014, *MNRAS*, 439, 1364
- Homan D. C., Wardle J. F. C., 1999, *AJ*, 118, 1942
- Intema H. T., van der Tol S., Cotton W. D., Cohen A. S., van Bemmell I. M., Röttgering H. J. A., 2009, *A&A*, 501, 1185
- Isoke N., Tashiro M., Makishima K., Iyamoto N., Suzuki M., Murakami M. M., Mori M., Abe K., 2002, *ApJ*, 580, L111
- Jaffe W., Perola G., 1973, *A&A*, 26, 423
- Jamrozny M., Machalski J., Mack K.-H., Klein U., 2005, *A&A*, 433, 467
- Kapinska A. D., Hardcastle M., Jackson C., An T., Baan W., Jarvis M., 2015, in Bourke T. L. et al., eds, *Proc. Advancing Astrophysics with the Square Kilometre Array, AASKA14, Unravelling lifecycles and physics of radio-loud AGN in the SKA Era*. SISSA, Trieste, PoS#173
- Kardashev N. S., 1962, *AJ*, 6, 317
- Kassim N. E. et al., 2007, *ApJ*, 172, 686
- Kataoka J., Stawarz L., 2005, *ApJ*, 622, 797
- Konar C., Hardcastle M. J., 2013, *MNRAS*, 436, 1595
- Konar C., Saikaid D. J., Jamrozny M., Machalski J., 2006, *MNRAS*, 372, 693
- Laing R. A., Bridle A. H., 2013, *MNRAS*, 432, 1114
- Laing R. A., Peacock J. A., 1980, *MNRAS*, 190, 903
- Laing R. A., Riley J. M., Longair M. S., 1983, *MNRAS*, 204, 151
- Leahy J. P., Perley R. A., 1991, *AJ*, 102, 537
- Longair M. S., 2011, *High Energy Astrophysics*. Cambridge Univ. Press, Cambridge

- Machalski J., Koziel-Wierzbowska D., Jamroz M., Saikia D. J., 2008, *ApJ*, 679, 149
- Machalski J., Jamroz M., Saikia D. J., 2009, *MNRAS*, 395, 812
- McNamara B. R., Nulsen P. E. J., 2012, *New J. Phys.*, 14, 055023
- Morganti R., Oosterloo T., Tsvetanov Z., 1988, *AJ*, 115, 915
- Morganti R., Fogasy J., Paragi Z., Oosterloo T., Orienti M., 2013, *Science*, 341, 1082
- Mullin L. M., Hardcastle M. J., Riley J. M., 2006, *MNRAS*, 372, 113
- Murgia M., Fanti C., Fanti R., Gregorini L., Klein U., Mack K.-H., Vigotti M., 1999, *A&A*, 345, 769
- Nandi S., Pirya A., Pal S., Konar C., Saikia D. J., Singh M., 2010, *MNRAS*, 404, 433
- Offringa A. R., de Bruyn A. G., Biehl M., Zaroubi S., Bernardi G., Pandey V. N., 2010, *MNRAS*, 405, 155
- Orrú E., Murgia M., Feretti L., Govoni F., Giovannini G., Lane W., Kassim N., Paladino R., 2010, *A&A*, 515, A50
- Owen F. N., Ledlow M. J., 1994, in Bicknell G. V., Dopita M. A., Quinn P. J., eds, *ASP Conf. Ser. Vol. 54, The First Stromlo Symposium: The Physics of Active Galaxies*. Astron. Soc. Pac., San Francisco, p. 319
- Pacholczyk A. G., 1970, *Radio Astrophysics. Nonthermal Processes in Galactic and Extragalactic Sources*. Freeman & Co., San Francisco
- Pandey V. N., van Zwieten J. E., de Bruyn A. G., Nijboer R., 2009, in Saikia D. J., Green D. A., Gupta Y., Venturi T., eds, *ASP Conf. Ser. Vol. 407, The Low-Frequency Radio Universe*. Astron. Soc. Pac., San Francisco, p. 384
- Rau U., Cornwell T. J., 2011, *A&A*, 532, 71
- Rengelink R. B., Tang Y., de Bruyn A. G., Miley G. K., Bremer M. N., Röttgering H. J. A., Bremer M. A. R., 1997, *A&AS*, 124, 259
- Scaife A. M. M., Heald G. H., 2012, *MNRAS*, 423, L30
- Scheers L. H. A., 2011, PhD thesis, Univ. Amsterdam
- Schoenmakers A. P., de Bruyn A. G., Röttgering H. J. A., van der Laan H., 2000, *MNRAS*, 315, 371
- Shelton D. L., Hardcastle M. J., Croston J. H., 2011, *MNRAS*, 418, 811
- Shulevski A. et al., 2015, *A&A*, 579, 27
- Sikora M., Stawarz L., Lasota J.-P., 2007, *ApJ*, 658, 815
- Sirothia S. K., Gopal-Krishna S., Wiita P. J., 2013, *ApJ*, 765, L11
- Spergel D. N. et al., 2003, *ApJS*, 148, 175
- Stroe A., Harwood J. J., Hardcastle M. J., Röttgering H. J. A., 2014, *MNRAS*, 445, 1213
- Swarup G., Ananthakrishnan S., Kapahi V. K., Rao A. P., Subrahmanya C. R., Kulkarni V. K., 1991, *Curr. Sci.*, 60, 95
- Tashiro M. et al., 1998, *ApJ*, 499, 713
- Tasse C., van der Tol S., van Zwieten J., van Diepen G., Bhatnagar S., 2013, *A&A*, 553, A105
- Tribble P., 1993, *MNRAS*, 261, 57
- van Haarlem M. P. et al., 2013, *A&A*, 556, A2
- van Weeren R. J., Williams W. L., Tasse C., 2014, *ApJ*, 793, 82
- Wardle J. F. C., Homan D. C., Ojha R., Roberts D. H., 1998, *Nature*, 395, 457
- Worrall D. M., Birkinshaw M., 2000, *ApJ*, 530, 719
- Young A., Rudnick L., Katz D., DeLaney T., Kassim N. E., Makishima K., 2005, *ApJ*, 626, 748

This paper has been typeset from a $\text{\TeX}/\text{\LaTeX}$ file prepared by the author.